Flexible Narrowband Ultraviolet Photodetectors with Photomultiplication Based on Wide Band Gap Conjugated Polymer and Inorganic Nanoparticles

Xiaoyu Zhang

A thesis

submitted in partial fulfillment of the

requirements for the degree of

Master of Science in Chemical Engineering

University of Washington

2018

Reading Committee:

Qiuming Yu, Chair

Samson Jenekhe

Program Authorized to Offer Degree:

Chemical Engineering

Abstract

Flexible Narrowband Ultraviolet Photodetectors with Photomultiplication Based on Wide Band Gap Conjugate Polymer and Inorganic Nanoparticles

Xiaoyu Zhang

Chair of the Supervisory Committee:
Professor Qiuming Yu
Department of Chemical Engineering

Lightweight and flexible ultraviolet (UV) photodetectors (PDs) have wide applications and have attracted more attention. PDs using organic and inorganic nanocomposites as active layers with a photodiode configuration could achieve photomultiplication and naorrowband photoresponse via the control of microstructure and thickness of active layers. Here, we fabricated flexible UV PDs on indium tin oxide (ITO) coated polyethylene terephthalate (PET) substrates with a nanocomposite active layer composed of ZnO nanoparticles blended with wide band gap conjugate polymer poly[(9,9-dioctylfluorenyl-2,7-diyl)-alt-co-(bithiophene)] (F8T2). As a result of wavelength-dependent penetration depth of light in the active layer, the fabricated flexible UV PDs showed two narrow response peaks at 360 and 510 nm under reverse biases in the external quantum efficiency (EQE) spectra with full-width at half-maximum (FWHM) less than 20 nm. Both responses exhibited greater than 100% EQE, indicating photomultiplication effect, while the UV response at 360 nm was 10 times stronger under -15 V bias. The fabricated flexible UV PDs

were bent under both tensile and compressive stress to a curvature of 2.1 cm^{-1}, each with 50 repetitions. The peak specific detectivity (D^*) only decreased by about 5% in total, the FWHM was well retained below 20 nm and the response speed remained almost constant after two types of bending, demonstrating mechanical flexibility and photoresponse stability of the fabricated flexible UV PDs. The photodiode configuration with nanocomposite active layers offers a promising route to make flexible and conformable narrowband, photomultiplication-type photodetectors for modern applications.

TABLE OF CONTENTS

LIST OF FIGURES

ACKNOWLEDGEMENTS

I want to expresse my sincere appreciation to my advisor Professor Qiuming Yu for her guidance and encouragement, my group members David Galvan, Monica Esopi, Gabriella Tosado, Erjin Zheng, Yi-Yu Lin, Chen Cai, Zhiyin Niu, and Hao Dong for their ideas, and my parents for their invaluable support.

Chapter 1. INTRODUCTION

This paper has been submitted to ACS Applied Materials & Interfaces by Xiaoyu Zhang, Erjin Zheng, Monica R. Esopi, Chen Cai, and Qiuming Yu*, with the title "Flexible Narrowband Ultraviolet Photodetectors with Photomultiplication Based on Wide Band Gap Conjugate Polymer and Inorganic Nanoparticles".

1.1 FLEXIBLE PHOTODETECTORS

Organic and organic-inorganic nanocomposite thin-film optoelectronic devices have attracted extensive attention because of their low cost, light weight, transparency and mechanical flexibility.[1] Flexible solar cells, light-emitting diodes (LEDs), and photodetectors (PDs) have all been successfully fabricated.[2-7] Ultraviolet (UV) PDs have a wide range of applications, such as chemical, environmental and biological analysis and monitoring, flame and radiation detection, astronomical studies, and optical communications. Flexible UV PDs have been mostly made based on the transistor configuration using one-dimensional binary metal oxide nanostructures,[8-11] two-dimensional nanomaterials,[12] or nanocomposite materials[4] as light absorbers between two metal electrodes. A variety of flexible substrates such as paper[8, 10], polyimide[9], polyethylene terephthalate (PET)[4, 12], textiles[10] and even curved bio-surface like leaves[10] have been used to make UV PDs and excellent mechanical flexibility has been demonstrated. Photodiode UV PDs with organic or nanocomposite active layer have the advantages of achieving photomultiplcation and narrowband photoresponse via the control of microstructure and thickness of the active layer. However, there are relatively limited reports on flexible UV PDs based on the photodiode configuration and using organic or organic-inorganic nanocomposite as the light absorbers, comparing to those on rigid substrates. Therefore, in this work, we made photodiode UV PDs on

PET substrates with nanocomposite active layers to achieve narrowband photoresponse at 360 nm with photomultiplication and demonstrated the photoresponse stability after tensile and compressive bending.

1.2 Rigid Nanocomposite Ultraviolet Photodetectors

Recently, photodiode UV PDs have been successfully fabricated on glass substrates with nanocomposite active layers composed of ZnO or TiO_2 nanoparticles (NPs) blended with semiconducting polymers.[13-15] By controlling the microstructure of NPs dispersed in a polymer matrix, polymer-NP blend films can take an advantage of the photomultiplication effect, where multiple charge carriers can be collected per incident photon and external quantum efficiency (EQE) values above 100% are achieved. UV PDs using ZnO NPs combined with poly-vinylcarbazole (PVK) as an active layer produced a remarkable peak EQE of 2.4×10^5 % and a peak specific detectivity (D*) of 3.43×10^{15} Jones under a reverse bias of -9 V and 360 nm illumination.[13] UV PDs with a nanocomposite active layer composed of TiO_2 NPs blended with 1,3-bis(N-carbazolyl)benzene (mCP) also demonstrated an EQE of 8.5×10^4 % and a peak D* of 3.72×10^{14} Jones under a reverse bias of -10 V and 351 nm illumination.[14]

1.3 Narrowband Photodetectors

Depending on the width of PD spectral response window, PDs are divided into two categories, broadband or narrowband. Narrowband PDs, which can detect a specific wavelength of light selectively, have wide applications in the fields of spectroscopy, fluorescence microscopy, environmental analysis and defense.[16-18] To achieve a narrowband photoresponse, a bandpass optical filter or a dichroic prism is often combined with a broadband PD that detects light with a wide range of wavelengths.[19-21] However, this approach not only limits the sensitivity and quantum

efficiency because of the reduction of light passing through the filter[20-21] but also complicates the design and increases the cost.[22] Recently, while plasmonic filters have attracted more attention as optical filters due to the ability to efficiently control light,[23-24] the absolute transmission, efficiency and pass bandwidth are still under improvement. Ideally, narrowband PDs can achieve the desired spectral response selectivity without the use of any external filter. Therefore, there is a growing interest in developing narrowband PDs. One approach is to develop new narrowband light absorbers such as organic semiconductors.[25-26] Another approach is to manipulate light absorption and carrier generation, transport and collection processes via selecting different active layer materials and varying the active layer thickness of photodiodes.[27-30] A new response mechanism called charge collection narrowing (CCN) was proposed to achieve the desired narrowband response by controlling the thickness of organic bulk-heterojunction photodiodes.[27] This is because charge collection depends on the location of generated excitons that are controlled by the light penetration depth at each wavelength and the band gap of the active layer materials. When the active layer is thick, the PD only responds to light with long wavelength and long penetration depth, so a narrowband response is achieved at long wavelength of the absorption edge of semiconductor polymer in the active layer, resulting in the narrowband response in the visible or near infrared region. Recently, highly narrowband perovskite photodetectors with tunable spectral response range have also been achieved through CCN.[28-30] Notably, the thick active layers required to achieve the narrowband responses inherently produce lower photocurrent values, so large applied voltages are required to achieve photomultiplication.[31-32]

In this work, flexible photomultiplication-type narrowband UV PDs with FWHM < 20 nm were successfully fabricated on PET substrates using poly[(9,9-dioctylfluorenyl-2,7-diyl)-alt-co-(bithiophene)] (F8T2) and ZnO NPs blended with a F8T2:ZnO weight ratio of 1:3 as the active

layer. The active layer is sandwiched between a transparent indium tin oxide (ITO) anode and an Al cathode, where Poly(3,4-ethylenedioxythiophene)-poly(styrenesulfonate) (PEDOT:PSS) is the hole-transport layer, and bathocuproine (BCP) works as the electron-transport/hole-blocking layer, for a full device structure of PET/ITO/PEDOT:PSS/F8T2:ZnO/BCP/Al, shown schematically in Figure 3.1a. The flexible PDs exhibited EQE spectra with two narrow response peaks under reverse bias due to the wavelength-dependent penetration depth of light in the active layer. 3-dimensional finite-difference time-domain (3D-FDTD) simulations were used to fully investigate and understand the EQE spectral shape. The PDs showed very low dark current density of 1.3 $\times 10^{-5}$ mA cm^{-2}, even under a strong reverse bias of -15 V. The champion EQE value produced by the PDs was 2,170% under 360 nm illumination and 220% under 510 nm illumination, both under -15 V bias. Moreover, the PDs were bent under both tensile and compressive stress, each with 50 repetitions. The peak specific detectivity (D^*) only decreased by about 5% in total, from 8.8×10^{11} Jones to 8.5×10^{11} Jones after tensile bending and to 8.3×10^{11} Jones after compressive bending. The FWHM was well retained below 20 nm and the response speed remained almost constant after tensile and compressive bending. Flexible narrowband photomultiplication-type UV photodetectors have potential applications in many fields, including chemical and biological detection, where light at specific wavelengths needs to be sensitively detected.

Chapter 2. EXPERIMENTAL METHODS

2.1 MATERIALS

ITO-coated PET (60 Ω sq^{-1}) with 150 Å thick ITO was purchased from Bayview Optics (Dover-Foxcroft, ME). Poly(3,4-ethylenedioxythiophene)-poly(styrenesulfonate) (PEDOT:PSS) solution (Clevios P VP AI 4083) was purchased from Heraeus (Hanau, Germany). Poly[(9,9-dioctylfluorenyl-2,7-diyl)-alt-co-(bithiophene)] (F8T2) was purchased from American Dye Source (Baie D'Urfe, Quebec, Canada) with molecular weight of 30K and polydispersity of 4.5. Anhydrous 1,2-dichlorobenzene (1,2-DCB) of 99.9% purity and 2,9-dimethyl-4,7-diphenyl-1,10-phenanthroline (BCP) of 99.99% purity were purchased from Sigma-Aldrich (St. Louis, MO). Aluminum pellets of 99.999% purity were purchased from R. D. Mathis (Long Beach, CA).

2.2 FILM FABRICATION

Glass substrate was cleaned by ultrasonication for 15 min each in soapy deionized (DI) water, DI water, acetone, and isopropyl alcohol, in sequence, and then by oxygen plasma cleaning at 100 W for 30 s. F8T2 was dissolved in DCB to make 40 mg/ml solution. ZnO NPs were prepared by hydrolysis method as mentioned in literature with a concentration of 200 mg/ml.[33] F8T2 solution (40 mg/ml) was blended with ZnO NPs (200 mg/ml) with a ratio of 1:3 and 1:2 by weight. Pure F8T2 and ZnO NP thin films and blended F8T2:ZnO (1:3, wt/wt) thin film were formed by spin-coating the precursor solutions on glass substrates at 1000 rpm for 30 s, followed by annealing at 80˚C for 10 min. All the fabrication steps were completed in a nitrogen-filled glovebox.

2.3 Film Analysis

UV-Vis absorption and photoluminescence spectra of pure and blended F8T2:ZnO NP films were collected using a Varian Cary 5000 UV-Vis-NIR spectrophotometer and a Horiba Fluorolog 3 Spectrofluorometer, respectively. Film thicknesses were measured using a KLA Tencor Alpha-Step 500 Profiler. Film morphology was characterized with tapping mode atomic force microscope (TM-AFM) using Digital Multimode AFM equipped with a Nanoscope Iva controller. The hydrodynamic diameter of the nanoparticles was determined using dynamic light scattering (DLS) with Malvern Zetasizer Nano. All the film analyses were performed in air.

2.4 Device Fabrication

ITO-coated PET substrates were cleaned by the same methods of ultrasonication and plasma treatment as the glass substrates used for film fabrication. The cleaned ITO/PET substrates were then fully mounted on glass substrates by double-sided kapton tape. PEDOT:PSS solution was filtered through a 0.45 μm nylon syringe filter and spin-coated onto a cleaned ITO/PET substrate at 3000 rpm for 60 s, followed by annealing at 120˚C for 30 min. The photoactive layer was obtained by spin-coating the F8T2:ZnO precursor solution at 1000 rpm for 30 s, followed by annealing at 80˚C for 10 min. The thickness of the photoactive layer was approximately 468 nm. A 10 nm thick BCP layer was deposited by thermal evaporation onto the photoactive layer. Finally, a 100 nm thick aluminum electrode was deposited via thermal evaporation with rectangular masks so that the active area of each device was 0.1 cm^2.

2.5 Device Characterization

Current density-voltage ($J-V$) measurements were obtained using a Keithley 2635B sourcemeter. Light was provided using a 150 W Xe lamp paired with an Oriel Cornerstone 130

Monochromator. The light intensity was measured using a Newport 1918-R Power Meter and Newport UV-Si Photodiode. For response speed measurements, a Stanford Research Systems SR540 optical chopper was used to provide light pulses, and the photoresponse was collected using a Tektronix TBS1052B Digital Oscilloscope. All device characterization measurements were performed in air.

2.6 ELECTROMAGNETIC SIMULATIONS

3-dimensional finite-difference time-domain (3D-FDTD, Lumerical FDTD Solutions) simulation was performed to obtain the electric field distribution of the devices. The simulated device is PET (100 nm)/ITO (100 nm)/PEDOT:PSS (40 nm)/F8T2:ZnO (1:3, wt/wt) (450 nm)/Al (100 nm), which has a similar structure as the experimentally fabricated devices. A light source in the range of 300-600 nm was positioned 600 nm below the PET layer of the device. The electric fields were collected with a field monitor, which is at a vertical cross section through the middle of the simulated device. Symmetric and anti-symmetric boundary conditions were used in the x and y directions, respectively, and perfectly matched layer boundary conditions were used in the z direction. The wavelength dependent refractive index, n, and extinction coefficient, k, of the active layer were obtained experimentally using a Woollam M-2000 Spectroscopic Ellipsometer.

Chapter 3. RESULTS AND DISCUSSION

3.1 Characterization of Pure and Blended F8T2 and ZnO NP Thin Films

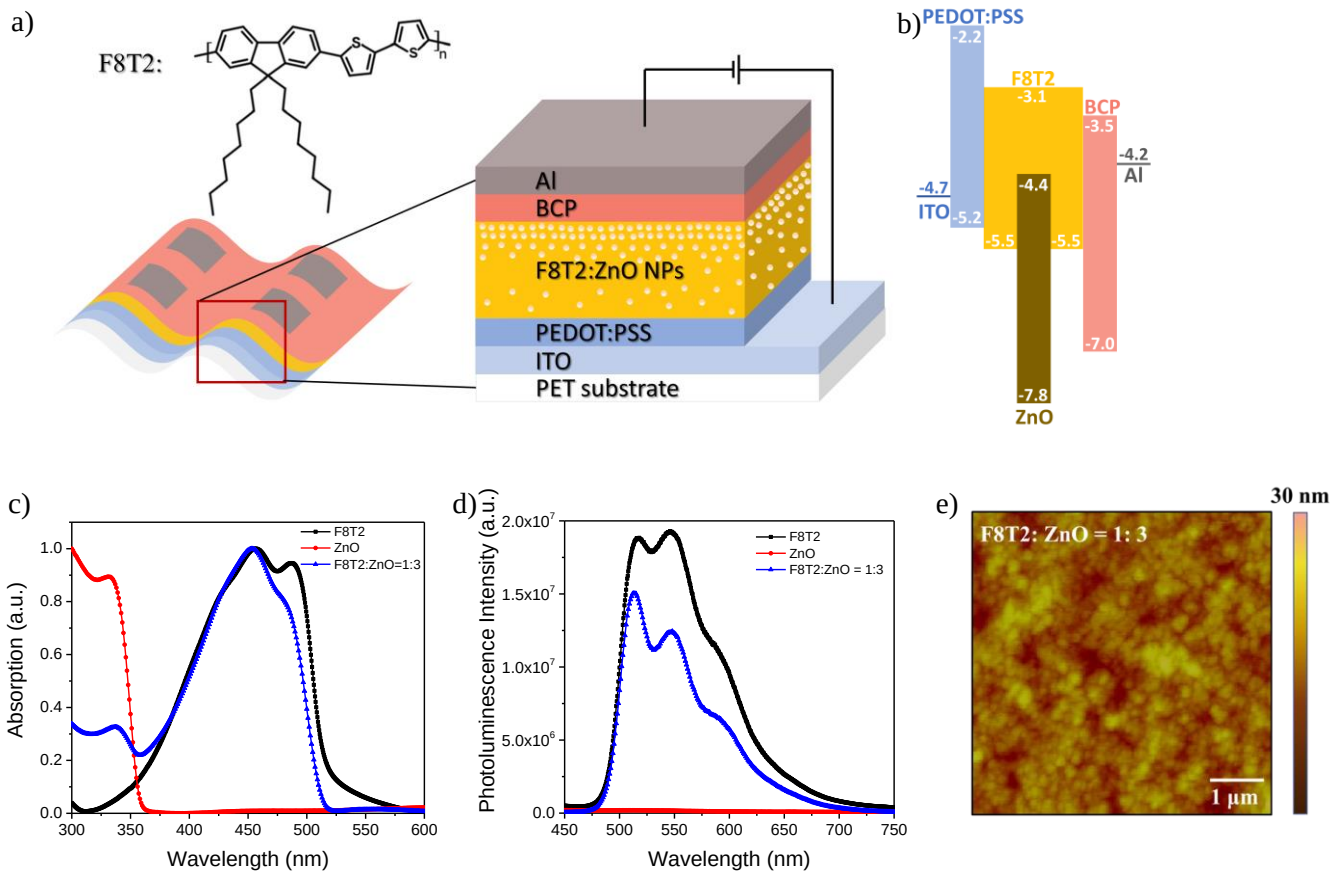

Figure 3. 1 a) Schematic illustration of the flexible narrowband UV photodetector structure and molecular structure of F8T2. b) Energy diagram of the materials deployed in the flexible narrowband UV photodetectors. c) UV–vis absorption spectra of pure F8T2 thin film (285 nm), ZnO NP thin film (441 nm), and the thin film of blended F8T2:ZnO with a 1:3 weight ratio (468 nm). Each spectrum was normalized to its own peak value. d) Photoluminescence spectrum of pure F8T2 thin film (285 nm), ZnO NP thin film (441 nm), and the thin film of blended F8T2:ZnO NPs with 1:3 weight ratios (468 nm). e) Topographic AFM image of the F8T2:ZnO NP (1:3, w/w) thin film (468 nm).

The liquid crystalline polymer F8T2 is a p-type semiconductor with a band gap of 2.4 eV and a hole mobility of 0.01 - 0.02 $cm^2 V^{-1} s^{-1}$.[34] ZnO NPs serve as UV absorbers due to their wide band gap of ~3.4 eV.[13, 35] Figure 3.1b presents the energy diagram for each layer in the fabricated devices. The absorption spectra of pure F8T2 and ZnO NP thin films and blended F8T2:ZnO NP thin film, each normalized to its own peak, are shown in Figure 3.1c. The ZnO NP thin film (441 nm) absorbs light with wavelengths shorter than 365 nm, which corresponds to the band gap of 3.4 eV. The F8T2 thin film (285 nm) shows strong absorption between 350 and 530 nm, with absorption peaks around 460 nm and 485 nm, and a soft cutoff around 525 nm. The F8T2:ZnO blend film, with a 1:3 weight ratio, shows strong UV absorption between 300 and 520 nm with a sharp cutoff around 520 nm. Comparing the absorption spectrum of the blend film to that of pure F8T2, the 485 nm peak becomes to a shoulder, and an obvious blue shift to 520 nm is observed in the blend film. This can be explained by the increased molecular disorder of F8T2 upon blending with ZnO NPs. Both pure F8T2 and blend F8T2:ZnO films were annealed at 80°C for 10 min, which is below the glass transition temperature of F8T2.[34, 36] The strong absorption peak at 485 nm would be originated in polarizing crystal growth of F8T2 in the film. The addition of ~ 10 nm ZnO NPs disrupts the F8T2 crystalline structure, resulting in the observed decrease and blue shift of the 485 nm peak due to isotropic behavior in amorphous phase.[36] An efficient quenching in photoluminescence is observed for the blend film compared to pure F8T2 (Figure 3.1d) indicating that charge separation occurs at F8T2:ZnO junctions.[37-38] The topographic atomic force microscopy (AFM) image of the blend film (Figure 3.1e) shows a smooth surface with a root mean square roughness of 2.5 nm.

3.2 Dark Current and Photocurrent Density versus Voltage

The current density versus voltage ($J-V$) curves measured in dark and under 360 nm monochromatic illumination with forward and reverse biases are shown in Figure 3.2a. Our nanocomposite PDs show low dark current density (J_D) of 1.3×10^{-5} mA cm^{-2} even at -15 V bias due to the lack of charge injection from the electrodes into the active layer. In dark conditions (Figure 3.2b), hole injection is suppressed due to the blocking capability of BCP and the large hole-injection barrier of 1.3 eV from the Al cathode into the highest occupied molecular orbital (HOMO) of F8T2. It should be noted that the electrons could be injected from the ITO anode into the conduction band of ZnO based on the relatively low electron-injection barrier of 0.3 eV, but the distribution of ZnO NPs in the active layer is such that ZnO NPs are predominantly located close to the Al cathode, so there is no physical path for electron injection from the ITO/PEDOT:PSS interface.[13]

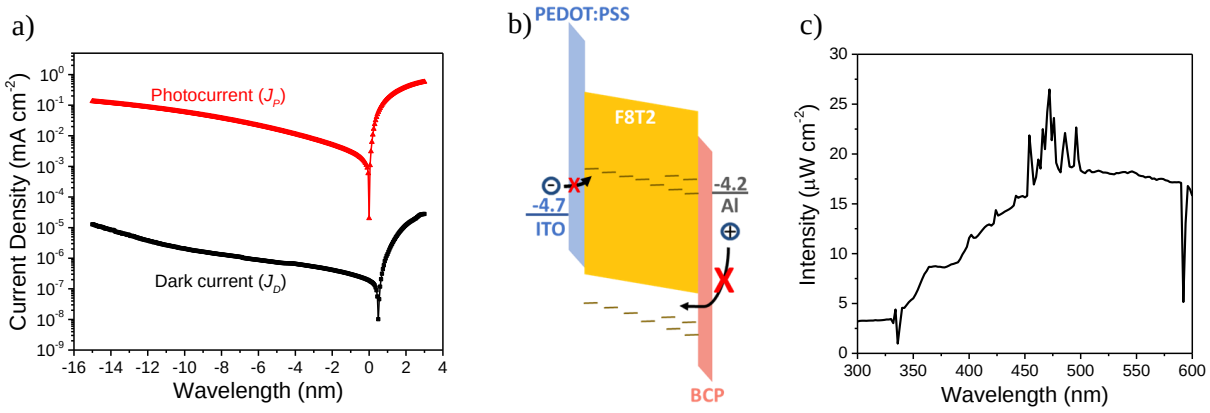

Figure 3. 2 a) The J-V curves in dark and under 360 nm light illumination. b) Energy diagram of the devices under reverse bias in the dark. c) The power curves for the xenon arc lamp used in this work.

The photocurrent density (J_P) is 4 orders of magnitude larger than the J_D at -15 V bias. This phenomenon indicates that the trapped electrons establish an accumulation of negative charge

from the external circuit under light illumination, which leading the hole injection and resulting in the remarkable photoresponse feature of the fabricated PDs. The fabricated PDs show reasonable rectification with a rectification ratio of >50 under ±3 V, indicating good diode behavior. Under forward bias, charge injection barriers are lowered and it is significantly easier for electrons and holes to be injected into the active layer than it is under reverse bias, where the injection barriers at the interfaces are increased and effectively block carrier injection.[15] The light intensity of the xenon lamp is plotted for each wavelength in Figure 3.2c.

3.3 Photomultiplication and Narrowband Response

The EQE is defined as the ratio of charge carriers collected to incident photons, and EQE values above 100% indicate that photomultiplication, the collection of multiple charge carriers per incident photon, has been achieved. The EQE spectra of the PDs under different reverse biases are shown in Figure 3.3a. Clearly, as the reverse bias increases, the EQE values increase to exceed 100%, exhibiting photomultiplication. The photomultiplication mechanism is illustrated in Figure 3.3b. Upon incorporation into the polymer active layer, ZnO NPs prefer to segregate towards the top of the active layer, near the cathode side, and therefore have very little interaction with the PEDOT:PSS interface.[13] This is essential for the effective utilization of the photomultiplication mechanism. Under illumination, electron-hole pairs are generated. The electrons are trapped in ZnO NPs due to a 1.3 eV energy barrier between the conduction band of ZnO and the lowest unoccupied molecular orbital (LUMO) of F8T2, while the holes can transfer to the F8T2 and diffuse towards the anode for collection. The hole injection that yields a photomultiplicative response relies on the band bending induced by electrons trapped in the ZnO NPs with an applied reverse bias. To effectively lower the barrier for hole injection, this band bending must occur physically near the Al cathode, from which the holes are injected. Therefore, to engage

photomultiplication the electrons must be trapped near the cathode, or the top of the active layer film, so the segregation of ZnO NPs towards the top of the active layer is essential to the success of the photomultiplication response.

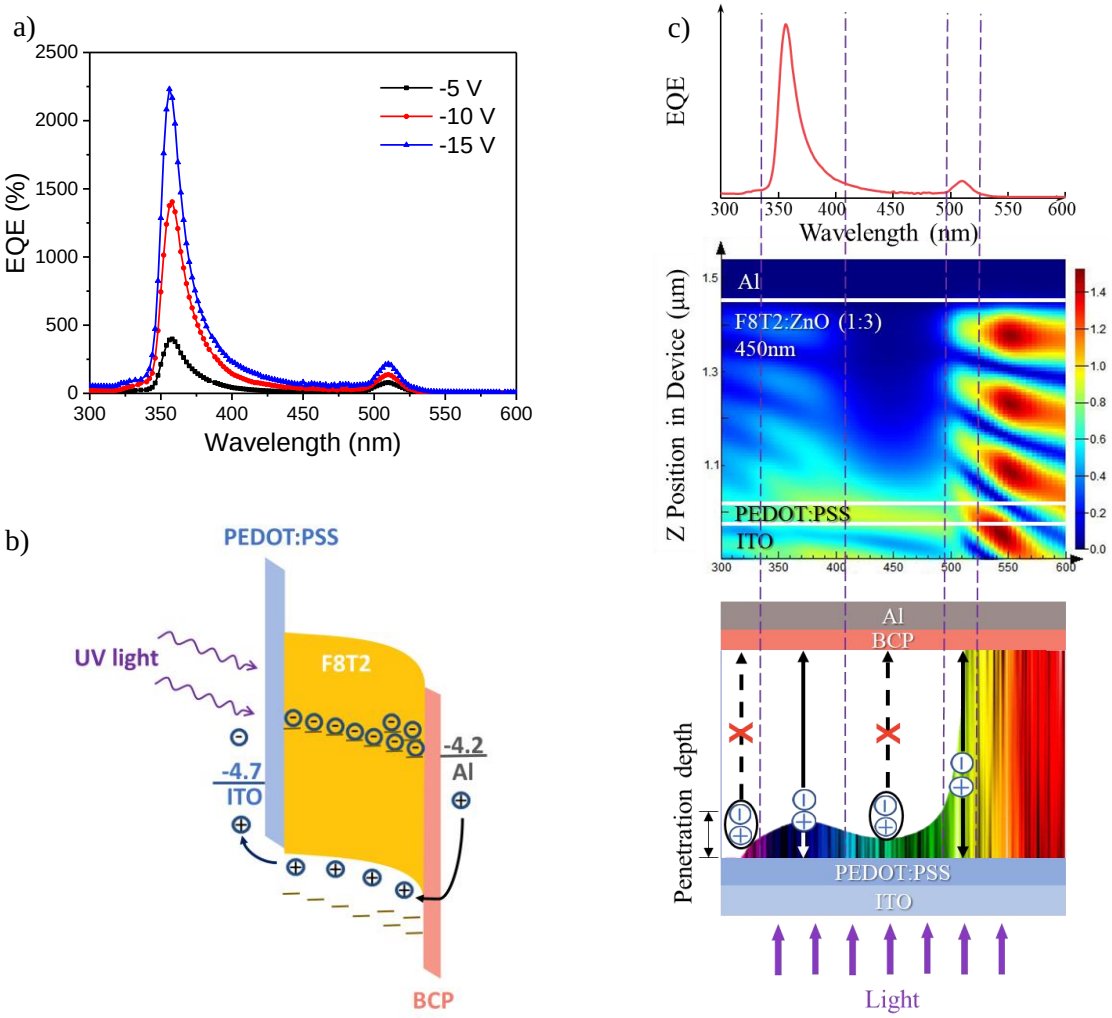

Figure. 3 a) EQE spectra of the photodetector under reverse biases of -5, -10 and -15 V. b) Energy diagram of the devices under reverse bias and illumination with electrons trapped in ZnO NPs close to the Al cathode, resulting in F8T2 band bending and hole injection from the Al cathode. c) Illustration of the narrowband photodetector working principle based on calculated light penetration depth and exciton generation in the active layer as well as the 3D-FDTD simulated electric field in the photodetector with 450 nm thick F8T2:ZnO (1:3, wt/wt) active layer.

Interestingly, the PDs exhibit EQE spectra with two narrow response peaks under reverse bias, each with a FWHM less than 20 nm. This EQE spectral shape can be ascribed to the wavelength-dependent penetration depth (L_p) in the active layer, which is shown in Figure 3.3c along with a sample EQE spectrum. The penetration depth is calculated by the following equation:

$$L_p = T\% \times \frac{\lambda}{4\pi k} \quad (1)$$

where $T\%$ is the transmittance (%) of ITO coated PET substrates (Figure 3.4a), λ is the wavelength of incident light, and k is the extinction coefficient of the thin film of blended F8T2:ZnO with a 1:3 weight ratio (Figure 3.4b). This penetration depth is used to explain the EQE spectral shape in various wavelength ranges.

Light with wavelengths between 300 nm to 340 nm penetrates shallow into the active layer near the PEDOT:PSS interface, which is composed primarily of F8T2 because of the preferentially segregation of ZnO NPs towards the top of the active layer. Since F8T2 does not absorb strongly in this range (Figure 3.1c), few excitons are generated. If an exciton is generated by light within this wavelength range, it is likely to recombine at the PEDOT:PSS interface, and has a very small chance of diffusing to any F8T2/ZnO interface, as they are concentrated towards the top of the active layer. Therefore, the EQE values are very low in this wavelength range. When the incident light has a wavelength between 335 nm and 410 nm, with a larger L_p (> 50 nm) the light reaches further into the active layer and can be absorbed by both F8T2 and ZnO NPs because both materials absorb within this wavelength range (Figure 3.1c). When excitons are generated in ZnO NPs, the electrons are trapped in the NPs while the holes can transfer to the F8T2 and diffuse towards the anode for collection. When excitons are generated in F8T2, they diffuse to F8T2/ZnO interfaces, where the electrons will transfer to the ZnO NPs and become trapped, while the holes can remain in the F8T2 and again diffuse towards and be collected at the ITO anode. With an applied reverse

bias, the trapped electrons in ZnO NPs near the Al cathode can bend the energy bands of the active layer downwards. This lowers the barrier for hole tunneling through the BCP blocking layer and enables significant hole injection from the Al cathode. These holes can then diffuse through the active layer, aided by the strong reverse bias and be collected by the ITO anode. This phenomenon further supports the idea that the ZnO NPs segregate and trap electrons near the Al cathode, as this is essential in the mechanism of hole injection under illumination and reverse bias.[39] The peak EQE in this wavelength range dramatically increases from 400% to 2,170% when the reverse bias increases from -5 V to -15 V (Figure 3.3a). This bias sensitivity is attributed to the enhanced hole tunneling injection and the improved hole transport in active layer resulting from the applied reverse bias.[38] The increase of EQE is also consistent with the increase of photocurrent shown in Figure 3.2a. For light in the spectral range between 410 nm and 490 nm, the light is absorbed strongly by F8T2 because it is within the peak absorption for pure F8T2 (Figure 3.1c). This strong absorption decreases the L_p of the light to less than 50 nm, so that it never reaches the upper portion of the active layer where the ZnO NPs are concentrated. Therefore, no charge trapping is achieved, and the photomultiplication mechanism is not engaged, so the EQE values in this region are rather low. Incident illumination with wavelengths between 490 nm and 525 nm can be absorbed only by the F8T2 in the active layer, not by ZnO NPs. The weak absorption leads to a long penetration depth and a bulk exciton generation throughout the entire active layer, and thus an EQE peak centered around 510 nm, which is due to the CCN mechanism previously discussed. Because the CCN mechanism is dependent primarily on the optical properties of the active layer, the EQE peak around 510 nm is much less sensitive to the applied bias compared to the EQE peak at 360 nm. It, therefore, increased from 80% to 220% under reverse biases of -5 V and -15 V, respectively.

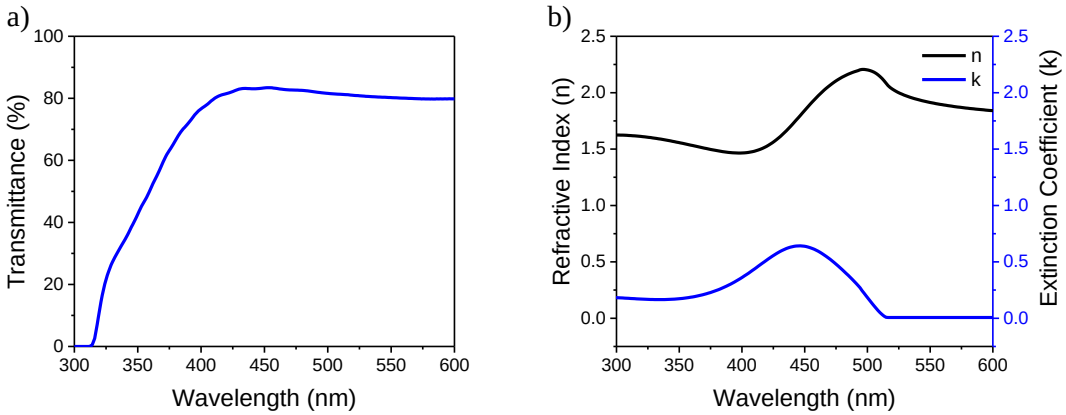

Figure 3. 4 a) Transmittance of ITO-coated PET substrates. b) Optical constants (refractive index n and extinction coefficient k) of F8T2:ZnO (1:3, wt/wt) blend film.

We also conducted 3D-FDTD simulations for a simulated device with the same active layer thickness and composition, 450 nm and an 1:3 wt/wt blend of F8T2:ZnO, as fabricated devices. The simulated electric field throughout a vertical cross-section of the device is shown in Figure 3.3c. Clearly, an electric field depletion region occurs between 410 nm and 490 nm due to strong F8T2 absorption, corresponding to low EQE in this region. Light below 410 nm induces stronger electric field close to the PEDOT:PSS interface, combined with charge injection discussed above, resulting in a strong EQE peak at 360 nm. Electric filed fringes appear above 510 nm because of no absorption in the active layer and combined with the CCN mechanism, result in the EQE peak at 510 nm. In summary, the champion EQE value of the PDs reached 2,170% under 360 nm light illumination or 220% under 510 nm light illumination, both at -15 V bias. Because the peak at 360 nm is more sensitive to bias than the peak at 510 nm, the narrowband response of the fabricated PDs becomes more UV selective as the bias is increased, and strong UV-selectivity can be achieved under large reverse biases. Most importantly, the FWHMs of EQE spectra of the highly narrowband photomultiplication-type PDs can be well retained at less than 20 nm under reverse

bias, indicating that the photogenerated electron distribution remains unchanged under increasing reverse bias.

Table 1. The key parameters of the pristine PDs under different reverse biases.

Bias (V)	J_D **(mA cm^{-2})**	I_{noise} **(pA Hz$^{-1/2}$)**	**EQE$_{360}$ (%)**	**FWHM$_{360}$ (nm)**	D^*_{360} **(Jones)**	**EQE$_{510}$ (%)**	**FWHM$_{510}$ (nm)**	D^*_{510} **(Jones)**
-5	7.3×10^{-7}	1.2	400	18	2.9×10^{11}	80	15	8.5×10^{10}
-10	2.1×10^{-6}	1.6	1400	19	7.7×10^{11}	140	15	1.1×10^{11}
-15	1.3×10^{-5}	2.3	2170	19	8.8×10^{11}	220	16	1.2×10^{11}

3.4 Specific Detectivity and Transient Photoresponse of the UV PDs

To further evaluate the device performance, the corresponding responsivity (R) and specific detectivity (D^*) were calculated. The R, as the ratio of photocurrent to intensity of incident light, was calculated according to the following expression:

$$R = \frac{EQE \times e}{h\nu} \tag{2}$$

where e is the electron charge, h is Planck's constant, and ν is the frequency of incident light. The R reached 6.39 A W^{-1} and 0.89 A W^{-1} at 360 nm and 510 nm, respectively, at -15 V bias (Figure 3.5a).

The D^* can be calculated according to the following equation:

$$D^* = \frac{R\sqrt{A}}{I_{noise}} \tag{3}$$

where R is the responsivity, A is the active area of the device, which is 0.1 cm^2 in this study, and I_{noise} is the noise current. Generally, the noise current is calculated as the summation of shot noise and thermal noise with the assumption that $1/f$ noise is negligible. Here, the noise current was calculated from the Fourier transform of measured dark current versus time, as shown in Figure 3.5b. This data suggests that the measured noise current is mainly influenced by $1/f$ noise at low

frequencies (f < 10 Hz), while the thermal noise dominates the noise current at high frequencies (f > 10 Hz). The noise current at 10 Hz is 1.2 pA $Hz^{-1/2}$ under -5 V bias and increases to 1.6 pA $Hz^{-1/2}$ and 2.3 pA $Hz^{-1/2}$ under -10 V bias and -15 V bias, respectively.

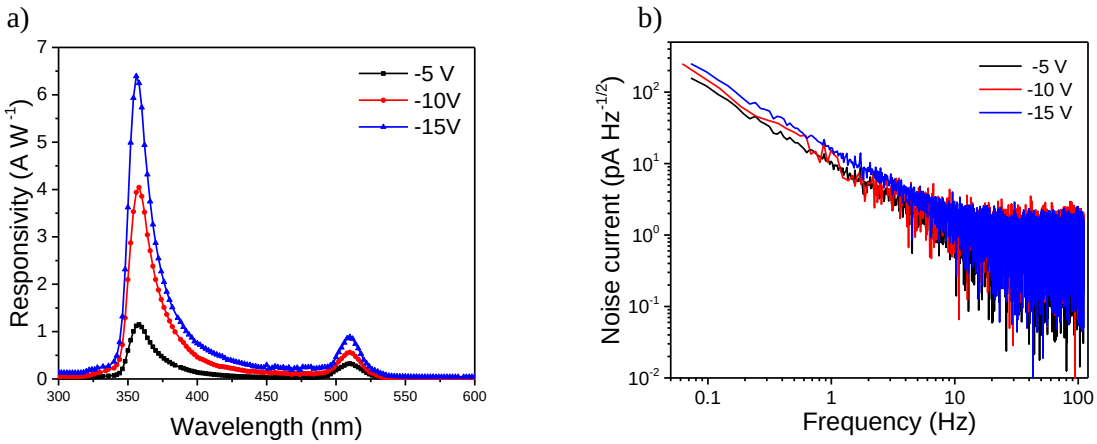

Figure 3. 5 a) Corresponding responsivity (R) of the photodetector under reverse biases of -5, -10 and -15 V. b) Noise current of the photodetector under reverse biases of -5, -10 and -15 V calculated from the Fourier transform of the dark current.

The D^* spectra of the fabricated PDs under reverse biases are shown in Figure 3.6a. The highest D^* is approximately 8.8×10^{11} Jones under 360 nm illumination and 1.2×10^{11} Jones under 510 nm illumination, both at −15 V bias. The D^* values in this work are comparable to those reported in the literature for similar systems. The highest D^* was approximately 1.3×10^{11} Jones under 650 nm light illumination at -10 V bias with a FWHM ~30 nm for the photodetector with a 2.5 μm thick P3HT:$PC_{71}BM$ (100:1, wt/wt) as the active layer,[31] and was 4.7×10^{10} Jones for 665 nm light at -10 V bias with a 4 μm thick P3HT: $PC_{61}BM$ (100:1, wt/wt) as the active layer.[32] The key parameters of the PDs under different biases are summarized in Table 1.

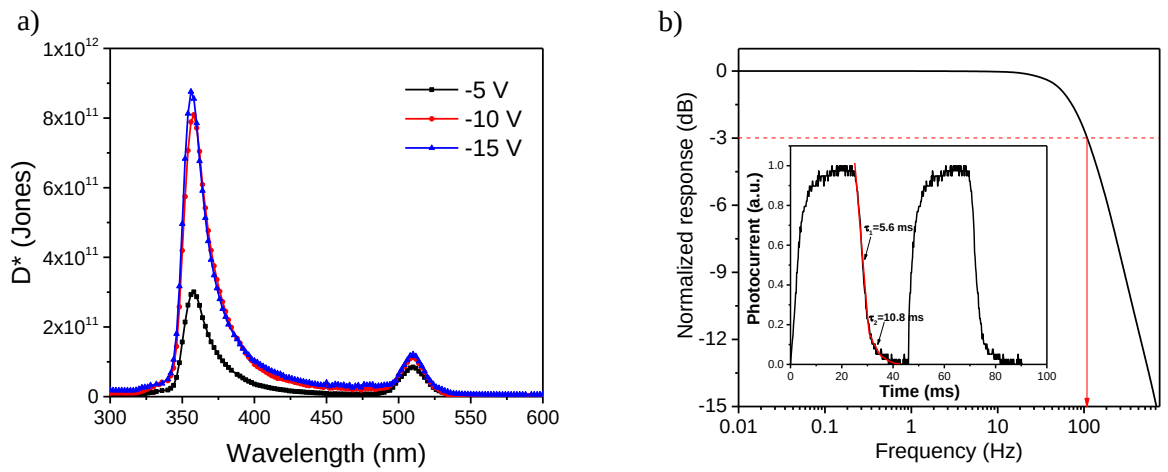

Figure 3. 6 a) Specific detectivities (D*) of the photodetector under reverse biases of -5, -10 and -15 V. b) Normalized response loss of the photodetector versus the input signal frequency at -15 V bias. The -3 dB point is specified with the dashed line. Inset: transient current density of the photodetector under 360 nm light illumination and applied -15 V bias.

The transient photocurrents of devices were measured under 360 nm incident light at -15 V bias, and are shown in the inset of Figure 3.6b. The transient photocurrent shows a rise time (output signal increases from 10% to 90% of the saturated output value) of 9.2 ms. As the response stabilizes, the excitons reach an equilibrium between recombination and electron trapping, yielding a saturated output signal. After switching off the illumination, the decay of the photocurrent has a fast fall time of 5.6 ms and a slow fall time of 10.8 ms. This phenomenon indicates the different trap depth of the nanoparticles in the nanocomposite due to the aggregation of ZnO NPs in polymer or the non-uniform feature of ZnO NPs.[13] When the excitation light is switched off, deeper traps need a longer time to release charge, resulting in the slower decay time of the device. The cutoff frequencies were calculated from the transient response times with varied illumination frequency. As shown in Figure 3.6b, the −3 dB cutoff frequency is 110 Hz at -15 V bias, which is comparable with nanocomposite PDs whose cutoff frequency range from 50 to 900 Hz.[15, 40]

3.5 PHOTORESPONSE AFTER TENSILE AND COMPRESSIVE BENDING

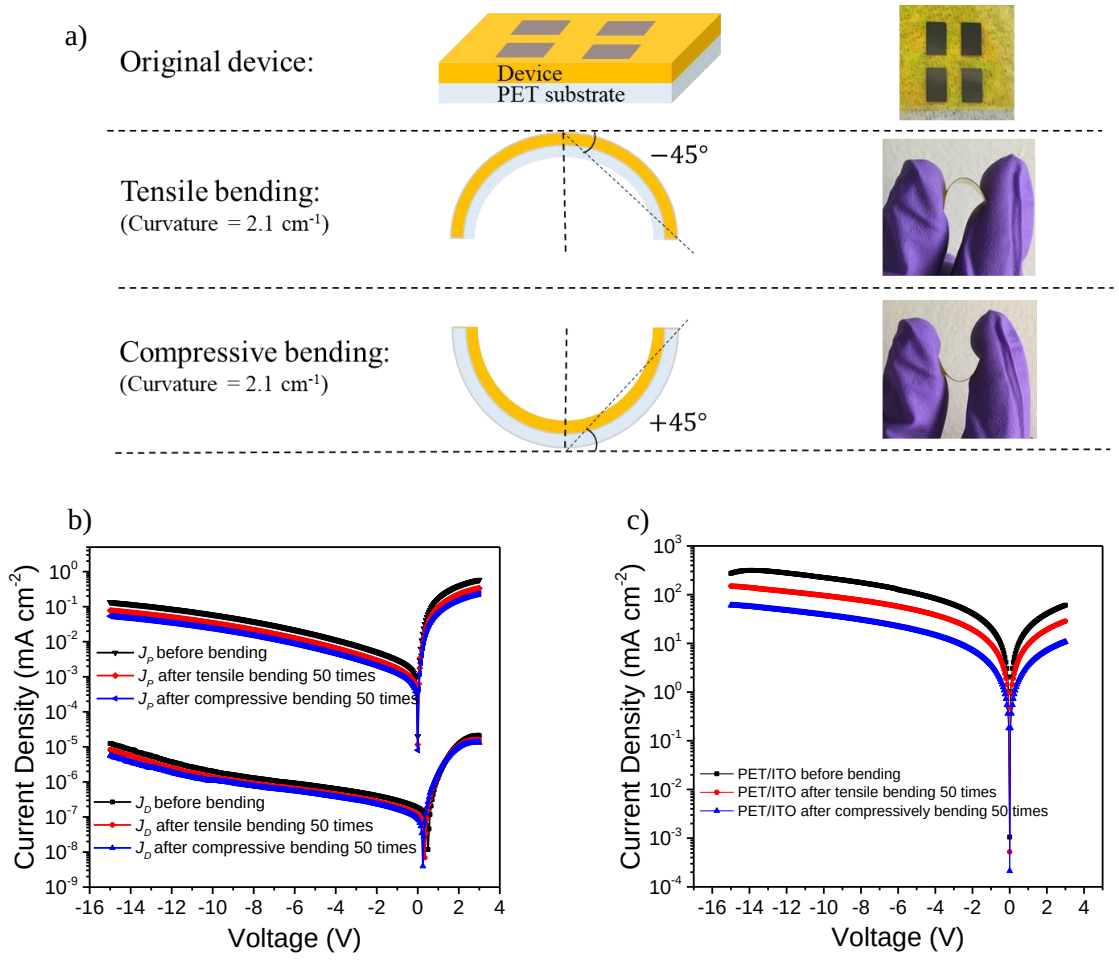

Figure 3. 7 a) Schematic and photographs of the pristine photodetector and the bending direction and angle for the photodetector. b) The J-V curves in dark and under 360 nm light illumination before and after tensile and compressive bending. c) The J-V curves of PET/ITO substrates before and after tensile and compressive bending.

A concern for flexible PDs is whether the performance degrades when they are subjected to mechanical deformations. Thus, it is practically important to study the device performance of the flexible devices both before and after bending. In this work, this study was conducted by bending the device to a specific bending angle and curvature in two different directions, resulting

in tensile and compressive stresses. As shown in Figure 3.7a, the device was bent under tensile stress and compressive stress, 50 times each. The device performance was evaluated in sequence on a freshly made device with no bending, after 50 times of tensile bending, and then after 50 times of compressive bending. The bending angle was ±45˚ (curvature of 2.1 cm^{-1}). Negative and positive angles are defined according to the bending direction, where the device undergoes tensile and compressive bending, respectively.

The $J-V$ curves were measured in the dark and under 360 nm monochromatic illumination before and after tensile and compressive bending (Figure 3.7b). Both dark current density (J_D) and photocurrent density (J_P) declined slightly after bending, but J_P is still 4 orders of magnitude larger than J_D at −15 V bias. This phenomenon signifies that the photodetector still shows a remarkable photoresponse even after both types of bending.

It should be noted that the fabricated PDs were not encapsulated and were bent in ambient air, so the dark current density decline could be due to the adsorption of molecular oxygen on the surface of the ZnO NPs resulting in the electron trap states and thus lower conductivity.[41-42] Under illumination or an applied forward bias, holes are introduced into the ZnO NPs, either through the generation of excitons or hole injection, which induces desorption of oxygen by recombining with the electron trapped at the surface oxygen defect. The freeing up electrons can lead to an increase in the conductivity of the ZnO NPs through a phenomenon called photoconductivity.[43] This is not the case for the devices in this work, which show a slight decrease in J_P after each type of bending. This might be due to a redistribution of ZnO NPs caused by the bending. ZnO NPs are predominantly located close to the cathode before bending. However, during the bending process, a small number of ZnO NPs near the Al may move away from cathode. Thus, fewer electrons will

become trapped near the Al cathode, resulting in a decrease in hole injections from the Al cathode and ultimately a decrease in photoresponse.

The decrease of dark and photocurrent density could also be due to the cracks of ITO after bending because of its intrinsic brittle characteristics arising from the ionic bond. The percentage change in electrical resistance increased with a higher number of bending cycles under the same bending angle and frequency.[44] We also measured the $J - V$ curves of ITO-coated PET substrates before and after tensile and compressive bending, each for 50 times. As shown in Figure 3.7c, the current density of ITO-coated PET substrates slightly decreased after tensile and compressive bending.

As it is one of the most important indicators of photodetector performance, the EQE spectra were measured at -15 V bias after tensile and compressive bending were each completed 50 times. As shown in Figure 3.8, the champion EQE values declined 20%, from 2,230% to 1,790%, after tensile bending, and further declined 23%, from 1,790% to 1,380%, after compressive bending, all measured under 360 nm illumination and -15 V bias. This decrease in EQE can be partially attributed to the adsorption of molecular oxygen on the surface of the ZnO NPs and the redistribution of electron traps in the active layer, and partially attributed to the decrease of conductivity of ITO due to the cracks, during bending. Meanwhile, because of the extremely weak absorption of ZnO NPs for wavelengths longer than 370 nm, the adsorption of molecular oxygen has a relatively small influence on the EQE spectra in this range. Thus, the EQE peak under 510 nm light illumination and -15 V bias, is decreased 17%, from 216% to 180%, after tensile bending and further decrease 22%, from 180% to 140%, after compressive bending.

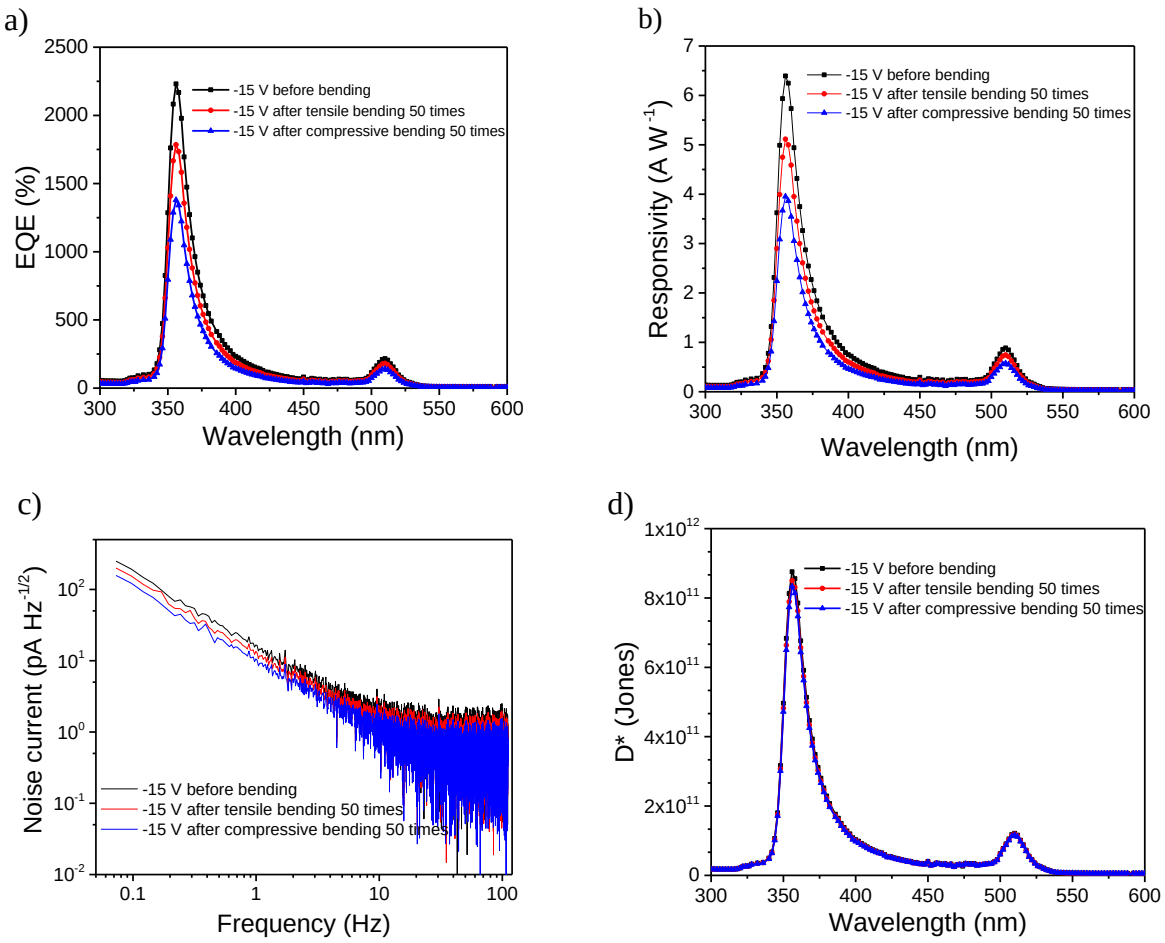

Figure 3. 8 a) EQE spectra of the photodetector before and after tensile and compressive bending at -15 V bias. b) Corresponding responsivity (R) of the photodetector before bending and after tensile and compressive bending at -15 V bias. c) Noise current of the photodetector before bending and after tensile and compressive bending at -15 V bias, calculated from the Fourier transform of the dark current. d) Specific detectivities of the photodetector before bending and after two types of bending at -15 V bias.

According to Equation 2, the corresponding R is proportional to EQE, thus, R decreases after bending. Shown in Figure 3.8b, the peak R under 360 nm illumination and -15 V bias is decreased 20% after tensile bending and further decreased 23% after compressive bending. The peak R at 510 nm is decreased 17% after tensile bending and further decreased 22% after

compressive bending. I_{noise} was measured at -15 V bias and is shown to decrease slightly from 2.3 pA Hz$^{-1/2}$ to 1.9 pA Hz$^{-1/2}$ after tensile bending and to 1.5 pA Hz$^{-1/2}$ after compressive bending. This decrease in I_{noise} (Figure 3.8c) is the results of the decrease in J_D after tensile and compressive bending (Figure 3.7b).

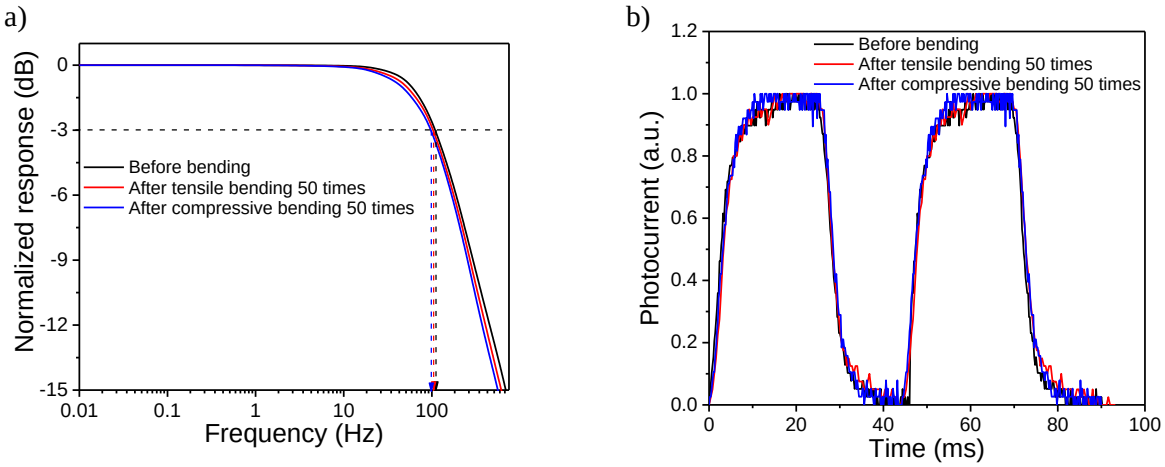

Figure 3. 9 a) Normalized response loss of the photodetector versus the input signal frequency before bending and after two types of bending. The -3 dB point is specified with the dashed line. b) Transient current density of photodetector under 360 nm light illumination before bending and after two types of bending.

Figure 3.8d shows the D^* at -15 V bias after both types of bending, compared to the D^* of a fresh, unbent device. Because both noise current and EQE are accounted for in D^*, the D^* values only decreased by about 5% under 360 nm illumination after both types of bending. The highest D^* under 360 nm illumination decreases from 8.8 × 10^{11} Jones to 8.5 × 10^{11} Jones and to 8.3 × 10^{11} Jones after tensile and compressive bending, respectively. On the other hand, the highest D^* under 510 nm light illumination decreases from 1.22 × 10^{11} Jones to 1.19 × 10^{11} Jones and to 1.16 × 10^{11} Jones after tensile and compressive bending, respectively. It is worth noting that the FWHM values of EQE spectra are well retained at less than 20 nm even after bending. Figure 3.9a shows

the transient photocurrents and response speed at -15 V bias after bending. The −3 dB cutoff frequency is only slightly decreased from 110 Hz to 104 Hz and 98 Hz after tensile and compressive bending, respectively. The rise time and fall times are unchanged after bending, as shown in Figure 3.9b. These results demonstrate the high mechanical flexibility and good photoresponse stability of the fabricated flexible photomultiplication-type narrowband PDs.

3.6 Characterization of Devices with Other F8T2: ZnO Active Layer Compositions

The UV PDs were also successfully fabricated on PET substrates using F8T2 and ZnO NPs blended with a F8T2:ZnO weight ratio of 1:2 and 1:10 as the active layer. Moreover, the active layers with a F8T2:ZnO weight ratio of 1:10 were annealed at two different temperature, 80°C and 100°C, for 10 min, which are both below the glass transition temperature of F8T2.

3.6.1 Devices with of F8T2: ZnO Weight Ratios of 1:2 as Active layers

The UV PDs were also successfully fabricated on PET substrates using F8T2 and ZnO NPs blended with a F8T2:ZnO weight ratio of 1:2 as the active layer. Similarly, The active layer is sandwiched between a transparent indium tin oxide (ITO) anode and an Al cathode, where Poly(3,4-ethylenedioxythiophene)-poly(styrenesulfonate) (PEDOT:PSS) is the hole-transport layer, and bathocuproine (BCP) works as the electron-transport/hole-blocking layer.

The absorption spectra of pure F8T2 and ZnO NP thin films and blended F8T2:ZnO NP thin film, each normalized to its own peak, are shown in Figure 3.10a. The F8T2:ZnO blend film, with a 1:2 weight ratio, shows strong UV absorption between 300 and 520 nm with a sharp cutoff around 520 nm. Similar to the F8T2:ZnO blend film with a 1:3 weight ratio, an obvious blue shift to 520 nm is observed in this blend film. Again, this can be explained by the increased molecular

disorder of F8T2 upon blending with ZnO NPs. Both pure F8T2 and blend F8T2:ZnO films were annealed at 80°C for 10 min, which is below the glass transition temperature of F8T2.[34, 36] An efficient quenching in photoluminescence is also observed for the blend film compared to pure F8T2 (Figure 3.10b) indicating that charge separation occurs at F8T2:ZnO junctions.[37-38] The topographic atomic force microscopy (AFM) image of the blend film (Figure 3.10c) shows a smooth surface with a root mean square roughness of 2.7 nm.

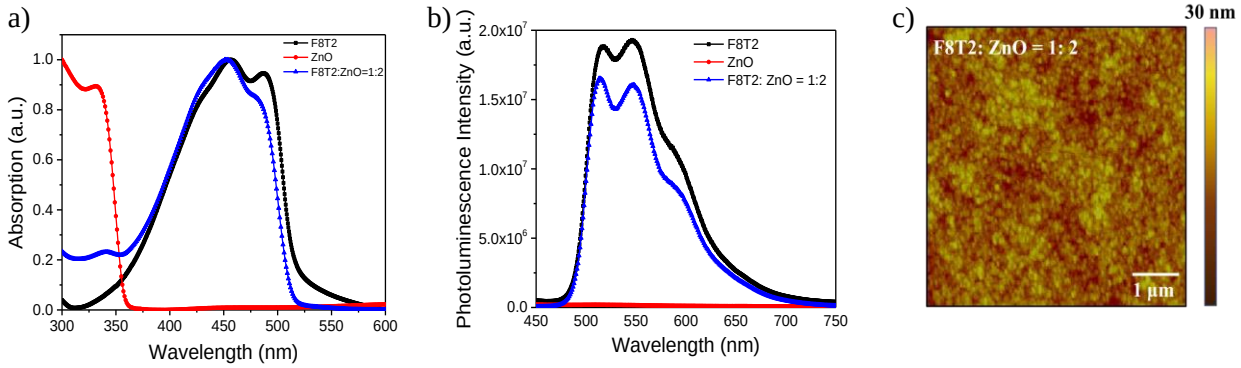

Figure 3. 10 a) UV–vis absorption spectra of pure F8T2 thin film (285 nm), ZnO NP thin film (441 nm), and the thin film of blended F8T2:ZnO with a 1:2 weight ratio (434 nm). Each spectrum was normalized to its own peak value. b) Photoluminescence spectrum of pure F8T2 thin film (285 nm), ZnO NP thin film (441 nm), and the thin film of blended F8T2:ZnO NPs with 1:2 weight ratios (434 nm). c) Topographic AFM image of the F8T2:ZnO NP (1:2, w/w) thin film (434 nm).

To study the device performance of the flexible devices both before and after bending, the device performance was evaluated in sequence on a freshly made device with no bending, after fixed the device on a cylinder (diameter = 3.6 cm) for 2 hrs, after 50 times of tensile bending, and then after 50 times of compressive bending, as shown in Figure 3.11a. The bending angle was ±45˚ (curvature of 2.1 cm^{-1}).

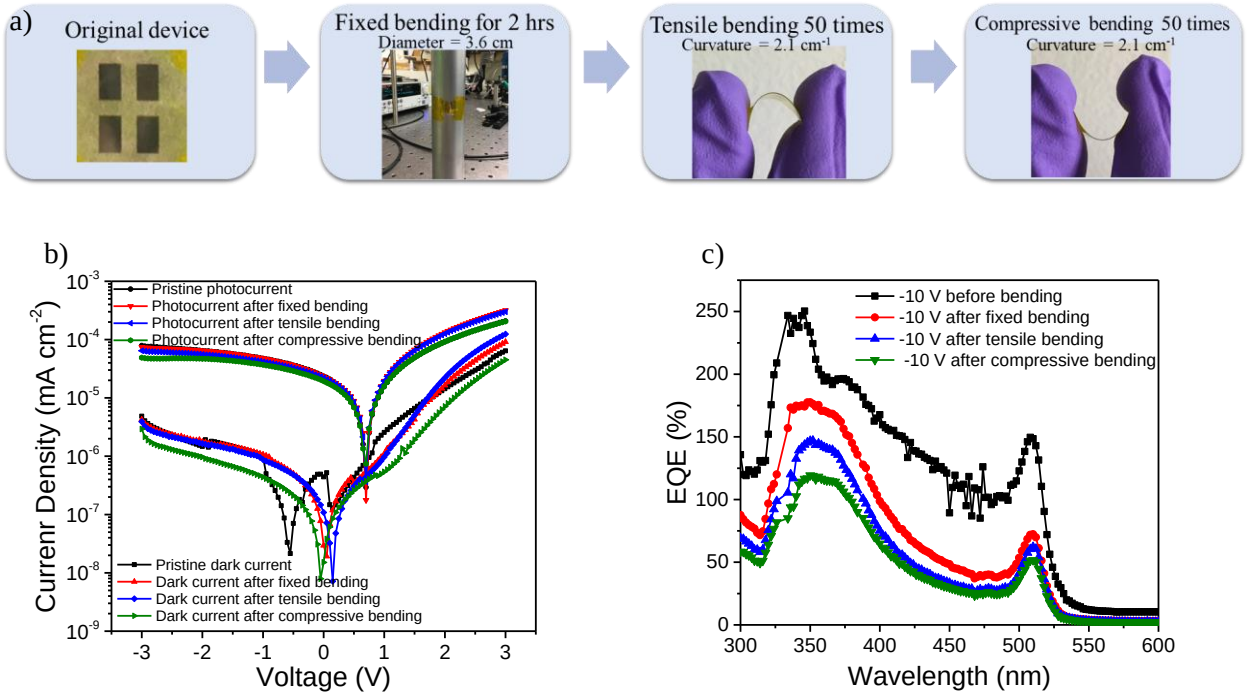

Figure 3. 11 a) Schematic and photographs of the pristine photodetector and the bending direction for the photodetector b) The J-V curves in dark and under 360 nm light illumination before and after three types of bending. c) EQE spectra of the photodetector before and after three types of bending at -10 V bias.

The $J-V$ curves were measured in the dark and under 360 nm monochromatic illumination before and after three types of bending (Figure 3.11b). Both dark current density (J_D) and photocurrent density (J_P) declined slightly after bending. As mentioned before, this decrease can be partially attributed to the adsorption of molecular oxygen on the surface of the ZnO NPs and the redistribution of electron traps in the active layer, and partially attributed to the decrease of conductivity of ITO due to the cracks, during bending. As it is one of the most important indicators of photodetector performance, the EQE spectra were measured at -10 V bias after three types of bending. As shown in Figure 3.11c, the EQE decreased after three types of bending, which

partially attributed to the redistribution of electron traps in the active layer, and partially attributed to the decrease of conductivity of ITO due to the cracks, during bending.

3.6.2 Devices with of F8T2: ZnO Weight Ratios of 1:10 as Active layers

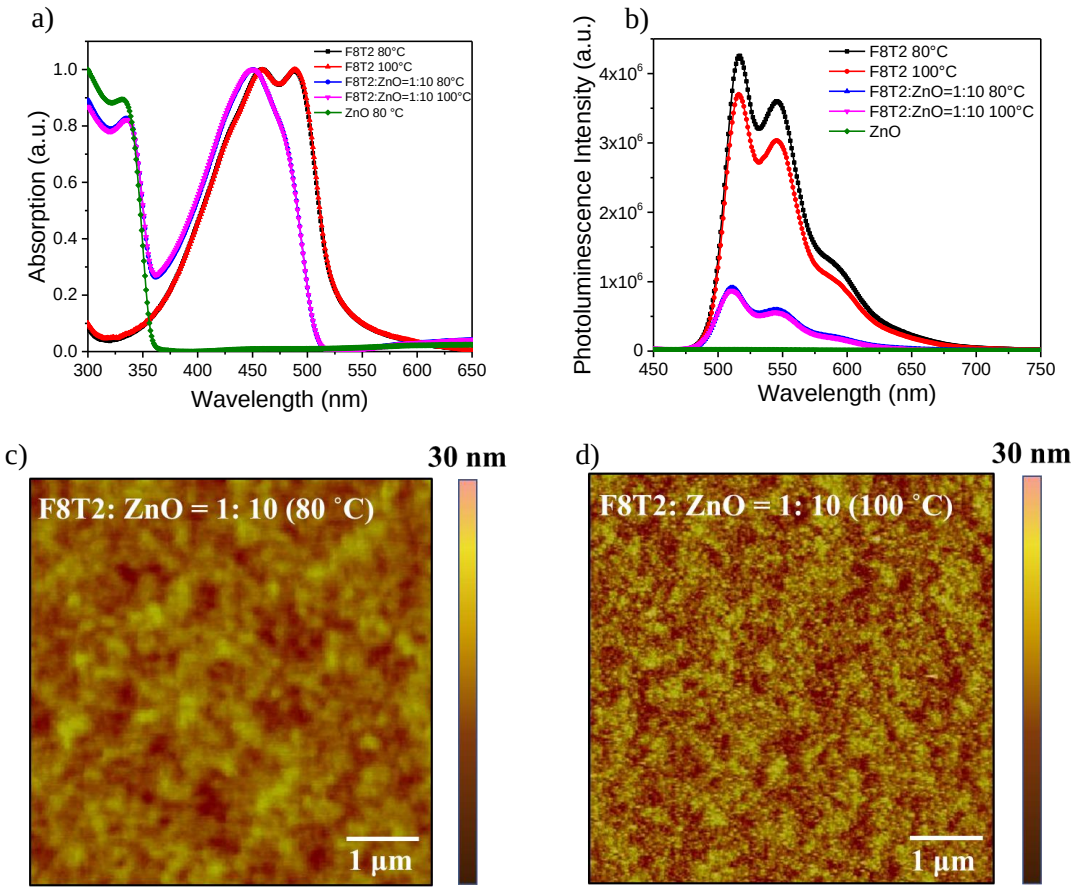

Figure 3. 12 a, b) UV–vis absorption spectra and photoluminescence spectrum of pure F8T2 thin film annealed at 80°C and 100°C (285 nm and 267 nm, respectively), the thin film of blended F8T2:ZnO with a 1:10 weight ratio annealed at 80°C and 100°C (434 nm and 421 nm, respectively), and ZnO NP thin film annealed at 80°C (441 nm). Each UV–vis absorption spectrum was normalized to its own peak value. c, d) Topographic AFM image of the F8T2:ZnO NP (1:10, w/w) thin film annealed at 80°C and 100°C (434 nm and 421 nm, respectively).

Additionally, the UV PDs were also fabricated on PET substrates using F8T2 and ZnO NPs blended with a F8T2:ZnO weight ratio of 1:10 as the active layer. Moreover, the active layers were annealed at two different temperature, 80°C and 100°C, for 10 min, which are both below the glass transition temperature of F8T2.

Effect of annealing condition on the electronic properties of pure F8T2 thin film and blend films were investigated. The absorption spectra of pure F8T2 and blended F8T2:ZnO NP thin film annealed at 80°C and 100°C, and ZnO NP thin films annealed at 80°C each normalized to its own peak, are shown in Figure 3.12a. By annealing condition at 80 °C and 100 °C below the glass transition, optical absorbance of pure F8T2 thin films and blend films remained unchanged. A slight quenching in photoluminescence is observed for both pure F8T2 thin films and blend films annealed at 100°C compared to those annealed at 80°C (Figure 3.12b) indicate the photo-induced charge generation of the polymer.[45] The topographic atomic force microscopy (AFM) image of the blend films (Figure 3.12c, d) show smooth surfaces with root mean square roughness of 4.7 nm when annealing at 80°C, and 2.9 nm when annealing at 100°C .

The $J-V$ curves were measured in the dark and under 360 nm monochromatic illumination from - 2 V to 2 V bias, as shown in Figure 3.13 a, b. Two devices shown similar dark current density from - 2 V to 2 V bias, while the photocurrent density of device with active layer (F8T2:ZnO = 1:10, wt/wt) annealed at 100°C was larger than that with active layer annealed at 80°C. The EQE spectra were measured at -1 V and - 3 V bias, as shown in Figure 3.13 c, d. Both of the devices shown EQE larger than 100% at -1 V bias indicating that photomultiplication has been achieved. Additionally, device with active layer (F8T2:ZnO = 1:10, wt/wt) annealed at 80°C shown lager EQE than that with active layer annealed at 100°C, both at -1 V and - 3 V bias.

Moreover, device with active layer (F8T2:ZnO = 1:10, wt/wt) annealed at 80°C had the FWHM below 20 nm, indicating the narrowband feature of the fabricated PDs.

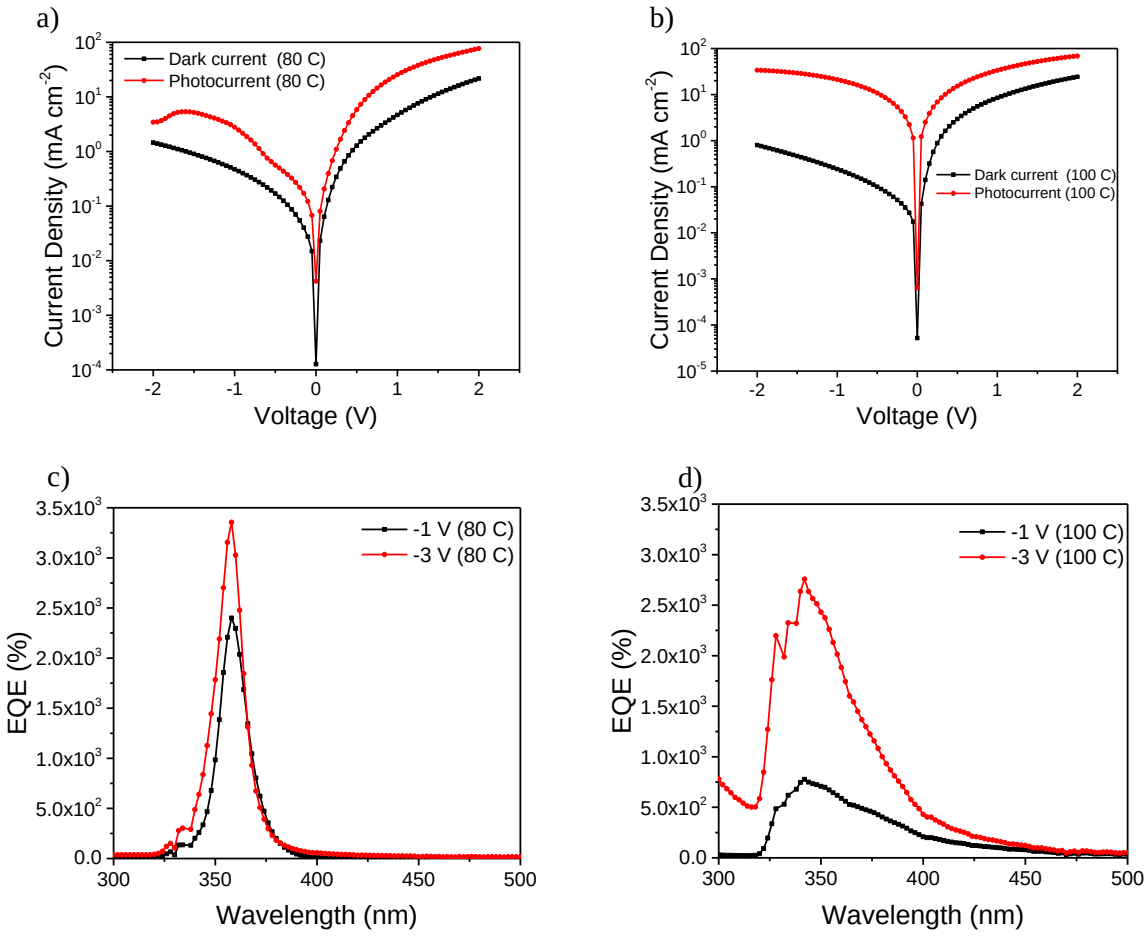

Figure 3. 13 a) The J-V curves in dark and under 360 nm light illumination for active layer (F8T2:ZnO = 1:10, wt/wt) annealed at 80°C. b) The J-V curves in dark and under 360 nm light illumination for active layer (F8T2:ZnO = 1:10, wt/wt) annealed at 100°C. c) EQE spectra of the photodetector with active layer (F8T2:ZnO = 1:10, wt/wt) annealed at 80°C. d) EQE spectra of the photodetector with active layer (F8T2:ZnO = 1:10, wt/wt) annealed at 100°C.

Chapter 4. CONCLUSION

We fabricated flexible photomultiplication-type narrowband UV photodetectors utilizing F8T2:ZnO nanocomposite active layers with a weight ratio of 1:3. The champion EQE value of the photodetectors reached 2,170% under 360 nm light illumination and 220% under 510 nm light illumination at -15 V bias, and both EQE peaks had FWHM values below 20 nm. Importantly, the flexible photodetectors showed good photoresponse stability after tensile and compressive bending, each with 50 repetitions. The highest D^* values only decreased by about 5%, from 8.8×10^{11} Jones to 8.5×10^{11} Jones after tensile bending and to 8.3×10^{11} Jones after compressive bending. Moreover, the FWHM was well retained below 20 nm and the response speed remained almost constant after two types of bending. Flexible narrowband photomultiplication-type UV photodetectors have potential applications in many fields, including chemical and biological detection, where light at specific wavelengths needs to be sensitively detected. The photodiode configuration with nanocomposite active layers offers a promising route to make flexible and conformable narrowband, photomultiplication-type photodetectors for modern applications.

REFERENCES

1. Jansen-van Vuuren, R. D.; Armin, A.; Pandey, A. K.; Burn, P. L.; Meredith, P., Organic Photodiodes: The Future of Full Color Detection and Image Sensing. *Adv. Mater.* **2016,** *28,* 4766-4802.

2. Kaltenbrunner, M.; White, M. S.; Glowacki, E. D.; Sekitani, T.; Someya, T.; Sariciftci, N. S.; Bauer, S., Ultrathin and Lightweight Organic Solar Cells with High Flexibility. *Nat. Commun.* **2012,** *3,* 770.

3. Yu, Z.; Niu, X.; Liu, Z.; Pei, Q., Intrinsically Stretchable Polymer Light-Emitting Devices Using Carbon Nanotube-Polymer Composite Electrodes. *Adv. Mater.* **2011,** *23,* 3989-3994.

4. Wang, X.; Song, W.; Liu, B.; Chen, G.; Chen, D.; Zhou, C.; Shen, G., High-Performance Organic-Inorganic Hybrid Photodetectors Based on P3ht:Cdse Nanowire Heterojunctions on Rigid and Flexible Substrates. *Adv. Funct. Mater.* **2013,** *23,* 1202-1209.

5. Yin, X.; Chen, P.; Que, M.; Xing, Y.; Que, W.; Niu, C.; Shao, J., Highly Efficient Flexible Perovskite Solar Cells Using Solution-Derived Niox Hole Contacts. *Acs Nano* **2016,** *10,* 3630-3636.

6. Zhou, L.; Xiang, H.-Y.; Shen, S.; Li, Y.-Q.; Chen, J.-D.; Xie, H.-J.; Goldthorpe, I. A.; Chen, L.-S.; Lee, S.-T.; Tang, J.-X., High-Performance Flexible Organic Light-Emitting Diodes Using Embedded Silver Network Transparent Electrodes. *Acs Nano* **2014,** *8,* 12796-12805.

7. Xiang, H.-Y.; Li, Y.-Q.; Zhou, L.; Xie, H.-J.; Li, C.; Ou, Q.-D.; Chen, L.-S.; Lee, C.-S.; Lee, S.-T.; Tang, J.-X., Outcoupling-Enhanced Flexible Organic Light-Emitting Diodes on Ameliorated Plastic Substrate with Built-in Indium–Tin-Oxide-Free Transparent Electrode. *Acs Nano* **2015,** *9,* 7553-7562.

8. Manekkathodi, A.; Lu, M. Y.; Wang, C. W.; Chen, L. J., Direct Growth of Aligned Zinc Oxide Nanorods on Paper Substrates for Low-Cost Flexible Electronics. *Adv. Mater*. **2010,** *22*, 4059-4063.

9. Liu, X.; Gu, L.; Zhang, Q.; Wu, J.; Long, Y.; Fan, Z., All-Printable Band-Edge Modulated Zno Nanowire Photodetectors with Ultra-High Detectivity. *Nat. Commun.* **2014,** *5*, 4007.

10. Huang, S.; Wu, H.; Zhou, M.; Zhao, C.; Yu, Z.; Ruan, Z.; Pan, W., A Flexible and Transparent Ceramic Nanobelt Network for Soft Electronics. *NPG Asia Mater.* **2014,** *6*, e86.

11. Chen, S.; Yu, M.; Han, W.-P.; Yan, X.; Liu, Y.-C.; Zhang, J.-C.; Zhang, H.-D.; Yu, G.-F.; Long, Y.-Z., Electrospun Anatase Tio2nanorods for Flexible Optoelectronic Devices. *RSC Adv.* **2014,** *4*, 46152-46156.

12. Hu, P.; Wang, L.; Yoon, M.; Zhang, J.; Feng, W.; Wang, X.; Wen, Z.; Idrobo, J. C.; Miyamoto, Y.; Geohegan, D. B.; Xiao, K., Highly Responsive Ultrathin Gas Nanosheet Photodetectors on Rigid and Flexible Substrates. *Nano Lett.* **2013,** *13*, 1649-1654.

13. Guo, F.; Yang, B.; Yuan, Y.; Xiao, Z.; Dong, Q.; Bi, Y.; Huang, J., A Nanocomposite Ultraviolet Photodetector Based on Interfacial Trap-Controlled Charge Injection. *Nat. Nanotechnol.* **2012,** *7*, 798-802.

14. Shao, D.; Yu, M.; Sun, H.; Xin, G.; Lian, J.; Sawyer, S., High-Performance Ultraviolet Photodetector Based on Organic-Inorganic Hybrid Structure. *ACS Appl. Mater. Interfaces* **2014,** *6*, 14690-14694.

15. Azadinia, M.; Fathollahi, M. R.; Mosadegh, M.; Boroumand, F. A.; Mohajerani, E., Improved Performance of Photoconductive Gain Hybrid Uv Detector by Trap State Engineering of Zno Nanoparticles. *J. Appl. Phys.* **2017,** *122*, 154501.

16. Zhou, L.; Wang, R.; Yao, C.; Li, X.; Wang, C.; Zhang, X.; Xu, C.; Zeng, A.; Zhao, D.; Zhang, F., Single-Band Upconversion Nanoprobes for Multiplexed Simultaneous in Situ Molecular Mapping of Cancer Biomarkers. *Nat. Commun.* **2015,** *6*, 6938.

17. Kelley, S. O.; Mirkin, C. A.; Walt, D. R.; Ismagilov, R. F.; Toner, M.; Sargent, E. H., Advancing the Speed, Sensitivity and Accuracy of Biomolecular Detection Using Multi-Length-Scale Engineering. *Nat. Nanotechnol.* **2014,** *9*, 969-980.

18. Matsumoto, A.; Tamura, A.; Koda, R.; Fukami, K.; Ogata, Y. H.; Nishi, N.; Thornton, B.; Sakka, T., On-Site Quantitative Elemental Analysis of Metal Ions in Aqueous Solutions by Underwater Laser-Induced Breakdown Spectroscopy Combined with Electrodeposition under Controlled Potential. *Anal. Chem.* **2015,** *87*, 1655-1661.

19. Konstantatos, G.; Clifford, J.; Levina, L.; Sargent, E. H., Sensitive Solution-Processed Visible-Wavelength Photodetectors. *Nat. Photon.* **2007,** *1*, 531.

20. Gautam, V.; Bag, M.; Narayan, K. S., Single-Pixel, Single-Layer Polymer Device as a Tricolor Sensor with Signals Mimicking Natural Photoreceptors. *J. Am. Chem. Soc.* **2011,** *133*, 17942-17949.

21. Higashi, Y.; Kim, K.-S.; Jeon, H.-G.; Ichikawa, M., Enhancing Spectral Contrast in Organic Red-Light Photodetectors Based on a Light-Absorbing and Exciton-Blocking Layered System. *J. Appl. Phys.* **2010,** *108*, 034502.

22. Park, H.; Dan, Y.; Seo, K.; Yu, Y. J.; Duane, P. K.; Wober, M.; Crozier, K. B., Filter-Free Image Sensor Pixels Comprising Silicon Nanowires with Selective Color Absorption. *Nano Lett.* **2014,** *14*, 1804-1809.

23. Yokogawa, S.; Burgos, S. P.; Atwater, H. A., Plasmonic Color Filters for Cmos Image Sensor Applications. *Nano Lett.* **2012,** *12*, 4349-4354.

24. Xu, T.; Wu, Y. K.; Luo, X.; Guo, L. J., Plasmonic Nanoresonators for High-Resolution Colour Filtering and Spectral Imaging. *Nat. Commun.* **2010,** *1*, 59.

25. Li, W.; Guo, H.; Wang, Z.; Dong, G., Narrowband Organic Photodiodes Based on Green Light Sensitive Squarylium. *J. Phys. Chem. C* **2017,** *121*, 15333-15338.

26. Jansen-van Vuuren, R. D.; Pivrikas, A.; Pandey, A. K.; Burn, P. L., Colour Selective Organic Photodetectors Utilizing Ketocyanine-Cored Dendrimers. *J. Mater. Chem. C* **2013,** *1*, 3532.

27. Armin, A.; Jansen-van Vuuren, R. D.; Kopidakis, N.; Burn, P. L.; Meredith, P., Narrowband Light Detection Via Internal Quantum Efficiency Manipulation of Organic Photodiodes. *Nat. Commun.* **2015,** *6*, 6343.

28. Lin, Q.; Armin, A.; Burn, P. L.; Meredith, P., Filterless Narrowband Visible Photodetectors. *Nat. Photon.* **2015,** *9*, 687-694.

29. Fang, Y.; Dong, Q.; Shao, Y.; Yuan, Y.; Huang, J., Highly Narrowband Perovskite Single-Crystal Photodetectors Enabled by Surface-Charge Recombination. *Nat. Photon.* **2015,** *9*, 679-686.

30. Saidaminov, M. I.; Haque, M. A.; Savoie, M.; Abdelhady, A. L.; Cho, N.; Dursun, I.; Buttner, U.; Alarousu, E.; Wu, T.; Bakr, O. M., Perovskite Photodetectors Operating in Both Narrowband and Broadband Regimes. *Adv. Mater.* **2016,** *28*, 8144-8149.

31. Wang, W.; Zhang, F.; Du, M.; Li, L.; Zhang, M.; Wang, K.; Wang, Y.; Hu, B.; Fang, Y.; Huang, J., Highly Narrowband Photomultiplication Type Organic Photodetectors. *Nano Lett.* **2017,** *17*, 1995-2002.

32. Miao, J.; Zhang, F.; Du, M.; Wang, W.; Fang, Y., Photomultiplication Type Narrowband Organic Photodetectors Working at Forward and Reverse Bias. *Phys. Chem. Chem. Phys.* **2017,** *19*, 14424-14430.

33. Pacholski, C.; Kornowski, A.; Weller, H., Self-Assembly of Zno: From Nanodots to Nanorods. *Angew. Chem. Int. Ed.* **2002,** *41*, 1188-1191.

34. Skompska, M., Hybrid Conjugated Polymer/Semiconductor Photovoltaic Cells. *Synth. Met.* **2010,** *160*, 1-15.

35. Monroy, E.; Omnes, F.; Calle, F., Wide-Bandgap Semiconductor Ultraviolet Photodetectors. *Semicond. Sci. Technol.* **2003,** *18*, 33-51.

36. Suzuki, A.; Suzuki, H.; Maruhashi, H.; Banya, S.; Akiyama, T.; Oku, T., Effect of Annealing on Photovoltaic Properties and Microstructure of Conventional and Inverted Organic Solar Cells Using Active Bilayer Based on Liquid-Crystal Semiconducting Polymer and Fullerene. *Int. J. Energy. Res.* **2014,** *38*, 1541-1550.

37. Yasuda, T.; Yonezawa, K.; Ito, M.; Kamioka, H.; Han, L.; Moritomo, Y., Photovoltaic Properties and Charge Dynamics in Nanophase-Separated F8t2/Pcbm Blend Films. *J. Photopolym. Sci. Technol.* **2012,** *25*, 271-276.

38. Esopi, M. R.; Calcagno, M.; Yu, Q., Organic Ultraviolet Photodetectors Exhibiting Photomultiplication, Low Dark Current, and High Stability. *Adv. Mater. Technol.* **2017,** *2*, 1700025.

39. Li, L.; Zhang, F.; Wang, J.; An, Q.; Sun, Q.; Wang, W.; Zhang, J.; Teng, F., Achieving Eqe of 16,700% in P3ht:Pc71bm Based Photodetectors by Trap-Assisted Photomultiplication. *Sci. Rep.* **2015,** *5*, 9181.

40. Shen, L.; Fang, Y.; Wei, H.; Yuan, Y.; Huang, J., A Highly Sensitive Narrowband Nanocomposite Photodetector with Gain. *Adv. Mater.* **2016,** *28*, 2043-2048.

41. Verbakel, F.; Meskers, S. C. J.; Janssen, R. A. J., Electronic Memory Effects in Diodes from a Zinc Oxide Nanoparticle-Polystyrene Hybrid Material. *Appl. Phys. Lett.* **2006,** *89*, 102103.

42. Verbakel, F.; Meskers, S. C. J.; Janssen, R. A. J., Electronic Memory Effects in Diodes of Zinc Oxide Nanoparticles in a Matrix of Polystyrene or Poly(3-Hexylthiophene). *J. Appl. Phys.* **2007,** *102*, 083701.

43. Jin, Y.; Wang, J.; Sun, B.; Blakesley, J. C.; Greenham, N. C., Solution-Processed Ultraviolet Photodetectors Based on Colloidal Zno Nanoparticles. *Nano Lett.* **2008,** *8*, 1649-1653.

44. Alzoubi, K.; Hamasha, M. M.; Lu, S.; Sammakia, B., Bending Fatigue Study of Sputtered Ito on Flexible Substrate. *J. Display Technol.* **2011,** *7*, 593-600.

45. Jo, J.; Vak, D.; Noh, Y.-Y.; Kim, S.-S.; Lim, B.; Kim, D.-Y., Effect of Photo- and Thermo-Oxidative Degradation on the Performance of Hybrid Photovoltaic Cells with a Fluorene-Based Copolymer and Nanocrystalline Tio2. *J. Mater. Chem.* **2008,** *18*, 654-659.